High-resolution phase-velocity maps using data from an earthquake recorded at regional distances by a dense broad-band seismic network

J. Arthur Snoke,[1] Linda M. Warren[2] and David E. James[3]

[1]*Department of Geosciences, Virginia Tech, Blacksburg, VA* 24061, *USA. E-mail:* snoke@vt.edu
[2]*Department of Earth and Atmospheric Sciences, Saint Louis University, Saint Louis, MO* 63108, *USA*
[3]*Department of Terrestrial Magnetism, Carnegie Institution of Washington, Washington, DC* 20015, *USA*

SUMMARY

The large regional earthquake (2008 February 21, $M = 6.0$) with epicentre near Wells, Nevada, occurred within a few hundred kilometres of the High Lava Plains (HLP) seismic experiment stations when the network was near its full deployment (>100 stations with 10–30 km station spacing). The Wells earthquake provides an excellent opportunity to address two questions: What is the effect of small epicentral distances on surface-wave analyses at periods that are used in the analysis of teleseisms? Can one take advantage of a high-density seismic network to obtain improved phase-velocity maps? As small epicentral distances may introduce systematic errors in the surface-wave analysis for longer periods, we test for such effects by generating synthetic waveforms at locations for all regional-distance stations recording the Wells earthquake. Analysis of the synthetics suggests that our surface-waves analyses can be applied for the Wells earthquake up to periods of $\sim$50 s. Applying the same method to data, we estimate two-station Rayleigh-wave fundamental-mode phase-velocities at selected periods and, for each acceptable path, assign the calculated phase velocity to the geographic location of the centre of the path. We contour the phase velocities for all path centres using a local gridding algorithm. The resulting maps for the Wells earthquake have well-constrained phase velocities up to 40–50 s period and allow us to see phase-velocity gradients not observed in earlier studies that used data from teleseisms or ambient noise tomography.

Key words: Time-series analysis; Composition of the continental crust; Surface waves and free oscillations; Seismic tomography; Computational seismology; Wave propagation.

1 INTRODUCTION

At maximum deployment, the High Lava Plains (HLP) seismic experiment had 104 broad-band stations with 10–30 km interstation spacing (Fig. 1a). The HLP station network spanned central and eastern Oregon, southwest Idaho, and northern Nevada and operated concurrently atop the footprint of the USArray Transportable Array (TA) regional grid, which had an average interstation spacing of $\sim$70 km across the western U.S. at that time. Together, these dense seismic station deployments afford an opportunity to image Earth structure and to test whether or not dense observations can be used to improve methodologies and imaging results.

Our earlier paper (Warren *et al.* 2008, henceforth, WSJ08) determined average Rayleigh-wave phase velocities and upper-mantle *S*-wave velocities for eight regions defined by station pairs aligned with great-circle paths (GCPs) from large, teleseismic earthquakes. The region with the largest number of paths (218 station-pairs from six earthquakes) was the northwest-southeast-oriented Group 2, which included almost all of the HLP network stations and is our current area of study (Fig. 1a). Only a small number of the HLP

stations were operating at that time, and only 51 of the station pairs included a HLP station. For that region, WSJ08 determined average phase velocities over the period range 16–128 s with estimated errors of less than 0.04 km s^{-1} for periods from 16 to 57 s (Table 1).

The focus of this paper is the analysis of a large regionally-recorded earthquake (2008 February 21; $M = 6.0$) near Wells, Nevada. The epicentre of this earthquake is in the southeast corner of our study area, and the earthquake occurred when the HLP network was near full deployment. As seen in Fig. 1(a), the HLP network stations have a fortuitous alignment for applying our two-station analysis procedures to this earthquake. Of 188 station pairs selected as described in Section 2.1, 179 included at least one HLP station.

Small distances may introduce systematic errors in the surface-wave analysis for longer periods (Wielandt & Schenk 1983; Lebedev *et al.* 2005; Bensen *et al.* 2007). Epicentral distances for stations from the Wells earthquake in our study area range from 65 to 787 km. Using synthetic-waveform modelling, we show in Section 3 that our surface-waves analyses can be applied for the Wells earthquake up to periods of $\sim$50 s for near-station epicentral
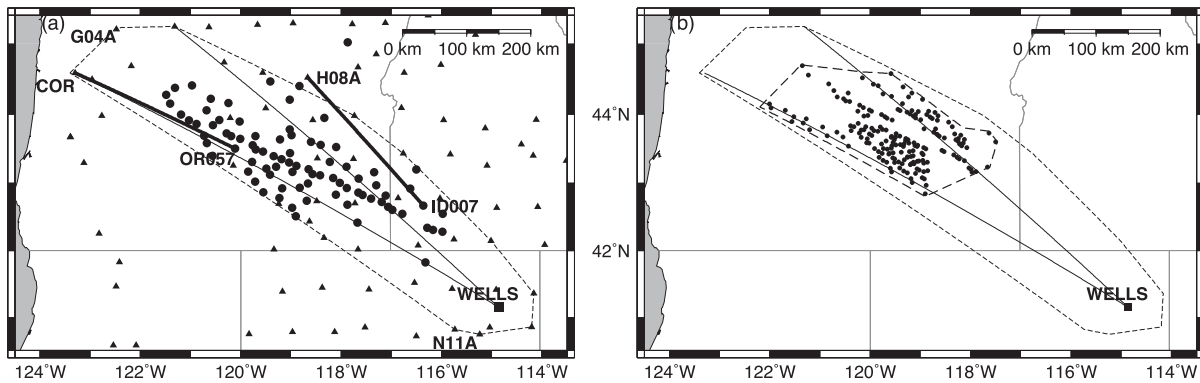
Figure 1. (a) Station distribution for the 2008 February 21 Wells earthquake. HLP stations are plotted as filled circles; stations from other networks are plotted as triangles. Thick solid lines indicate interstation paths between labelled stations referred to in the text. (b) Path centres (plotted as circles) for the Wells earthquake. In both subfigures, the Wells epicentre is shown as a black square, and two epicentre-station great-circle paths are shown as thin straight lines. The thin dashed line outlines the WSJ08 Group 2 (our study area), and the thick dashed line bounds the 188 interstation-path centres. Very thin solid lines are the state boundaries.

Table 1. Phase velocities (c) and calculated standard deviations (σ) at selected periods (T) in seconds for the reference-model phase velocities (c_r) (WSJ08, Group 2), and the calculated $\bar{c}$, σ and $\underline{s}$ from the analysis of both the synthetics (1-mode and 100-mode) and real data for the 2008 Wells earthquake. The reference-model phase velocities are constrained only down to a period of 16 s, so values given for shorter periods are extrapolations based on fitting the model. See Appendix for definitions.

	Group 2		1-mode synthetics			100-mode synthetics			Wells data		
T (s)	c_r (km s^{-1})	σ (km s^{-1})	$\bar{c}$ (km s^{-1})	σ (km s^{-1})	$\underline{s}$ (km s^{-1})	$\bar{c}$ (km s^{-1})	σ (km s^{-1})	$\underline{s}$ (km s^{-1})	$\bar{c}$ (km s^{-1})	σ (km s^{-1})	$\underline{s}$ (km s^{-1})
6.0	2.886		2.886	0.000	0.001	2.887	0.007	0.011	2.908	0.0339	0.0074
6.5	2.919		2.919	0.000	0.001	2.918	0.007	0.011	2.946	0.0391	0.008
7.0	2.953		2.953	0.000	0.001	2.952	0.005	0.010	2.978	0.0409	0.0083
7.6	2.987		2.987	0.000	0.001	2.988	0.005	0.009	3.008	0.0285	0.0085
8.4	3.021		3.021	0.000	0.000	3.021	0.005	0.008	3.039	0.0271	0.0066
9.1	3.051		3.051	0.000	0.000	3.050	0.004	0.006	3.07	0.0299	0.0055
10.0	3.083		3.084	0.000	0.000	3.084	0.003	0.006	3.102	0.0332	0.0054
11.1	3.121		3.121	0.001	0.001	3.121	0.004	0.006	3.136	0.0404	0.0054
12.5	3.168		3.168	0.001	0.001	3.169	0.005	0.012	3.177	0.0432	0.006
13.8	3.216		3.216	0.001	0.001	3.216	0.005	0.013	3.219	0.0456	0.0087
15.5	3.278		3.278	0.001	0.002	3.277	0.005	0.007	3.271	0.0518	0.0131
17.7	3.357	0.036	3.357	0.001	0.002	3.357	0.003	0.004	3.341	0.0533	0.0181
20.5	3.452	0.036	3.450	0.002	0.003	3.452	0.002	0.003	3.434	0.0472	0.022
23.3	3.527	0.031	3.525	0.001	0.002	3.527	0.002	0.002	3.523	0.0297	0.0157
26.9	3.597	0.025	3.597	0.003	0.003	3.600	0.003	0.003	3.594	0.029	0.0106
32.0	3.658	p.023	3.663	0.005	0.005	3.666	0.003	0.005	3.651	0.0269	0.0103
39.4	3.709	0.026	3.722	0.006	0.007	3.722	0.002	0.007	3.706	0.024	0.0134
46.5	3.741	0.028	3.756	0.003	0.008	3.752	0.003	0.009	3.749	0.0275	0.0126
56.9	3.779	0.035	3.790	0.002	0.012	3.782	0.005	0.011	3.793	0.0326	0.0129
73.1	3.835	0.052	3.828	0.009	0.023	3.820	0.013	0.024	3.839	0.0339	0.0242
102.4	3.946	0.062	3.885	0.015	0.040	3.862	0.028	0.053	3.931	0.0446	0.053
128.0	4.060	0.063	3.954	0.027	0.053	3.920	0.027	0.045	4.024	0.0909	0.1163

distances greater than 200 km. Guided by our results with synthetics, in Section 4 we apply our procedures to the Wells data.

2 INTERSTATION PHASE VELOCITIES AND PHASE-VELOCITY MAPS

We determine interstation phase velocities using methods described in WSJ08 and in our earlier studies (Snoke & James 1997; Snoke & Sanbridge 2002; Larson *et al.* 2006). After reviewing the methodology and comparing group-velocity spectra from regional and teleseismic earthquakes, we extend the methodology to produce phase-velocity maps.

2.1 Interstation phase-velocity determinations

To minimize multipathing, the WSJ08 selection procedure for earthquakes included only teleseismic surface waves that cross tectonic boundaries at near-normal incidence. For each earthquake, the vertical-component seismograms from all available stations in our study region were processed by correcting for the instrument response, decimating (if needed) to 1 sps ($\delta t = 1$ s), and integrating to displacement. Next, we used frequency-time analysis (FTAN; Dziewonski *et al.* 1969; Nyman & Landisman 1977; Levshin *et al.* 1989) at a representative subset of stations to identify the appropriate ranges of group velocities and periods for each earthquake based on the quality of the group-velocity spectra. For example, the contour patterns in the FTAN plot (Fig. 2a) for a 2006
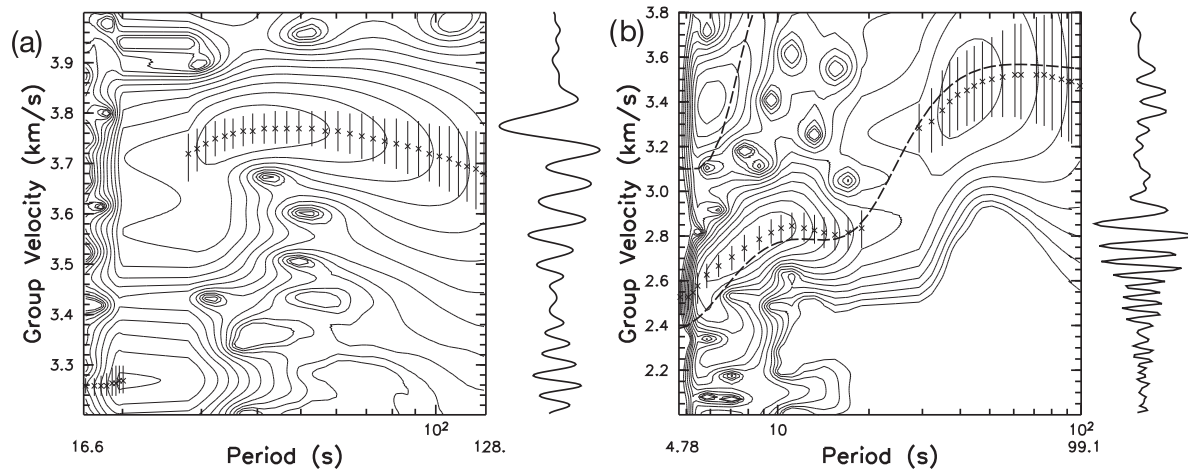
Figure 2. Group velocity versus period for the vertical-component waveforms (a) at station N11A from one of WSJ08's Aleutian earthquakes (2006 June 14; $M = 6.4$) with an epicentral distance of 5114 km, and (b) at station G04A from the Wells earthquake with an epicentral distance of 765 km. Station locations are shown in Fig. 1(a). The instrument-corrected seismogram (shown to the right in each subfigure) is narrow band-pass filtered at 37 centre frequencies and the quadrature traces (envelopes) are calculated and contoured. Adjacent contours correspond to a factor of 2. The x's are computer-picked quadrature-trace amplitude maxima for each period, and the vertical lines span ±1 dB. The plotted period extremes are indicated. In (b), the dashed lines show the Rayleigh-wave fundamental- and first higher-mode group-velocity for the velocity model used to create the synthetics (not corrected for the depth or focal mechanism and extrapolated for periods below 16 s). The calculated group velocities have been corrected for a group delay of 2.5 s.

Aleutian earthquake indicate well-constrained group-velocities over the range 3.00–3.95 km s^{-1} and the period range 16–128 s, with a spectral gap around 20 s period.

We filtered all vertical component seismograms for each event in both time and frequency. The minimum and maximum times were based on the chosen range of group velocities. We used a time-domain filter that is flat over the group-velocity-determined time window and cosine-tapered to zero at both ends over a time interval of 15 per cent of the selected time window. For this event at station N11A, with an epicentral distance of 5114 km, the time window is $1.3 \times (1705 - 1295) = 533$ s. A similar filter was applied in the frequency domain. Because our analysis uses correlations and coherence among waveforms, we used the same filtering for all seismograms.

For the Wells earthquake recorded at regional distances, group velocities are well constrained down to periods below 7 s (Fig. 2b). The reference-model group velocities at station G04A (shown in Fig. 1b) are plotted for both the fundamental and first higher mode. Because both the epicentre and the station are in our area of study, the group velocities are 'pure path' in contrast with recordings from teleseisms.

Station pairs are identified that have an interstation distance ≥ 200 km and a common GCP such that the differential station–station and distant-station-epicentre backazimuth is $\leq 3°$. To minimize the potential for cycle-skipping and to make a first pass at including dispersion between the stations, the near-station waveform is time-shifted to the far-station epicentral distance at each frequency using phase velocities corresponding to a reference velocity model. For this study, we use the Group 2 phase-velocity model from WSJ08 as the reference phase-velocity model (Table 1).

The calculation of the interstation phase velocities is an extension of the coherency-based procedure developed by Herrmann (1991) based in turn on Jenkins & Watts (1968) and Shumway (1988). The calculations are done in the frequency domain working with the transformed waveforms from the near station (after the waveform has been time-shifted) and from the far station.

We refer the reader to WSJ08 for the details involved in the calculations of the autocorrelations and cross correlations, as well

as the assumptions used to derive estimates of the cross spectra. At each discrete frequency ω_k, the phase velocity ($c(\omega_k)$) and its estimated error ($\Delta c(\omega_k)$) are calculated from

$$\frac{1}{c(\omega_k)} = \frac{1}{c_r(\omega_k)} - \frac{\phi(\omega_k)}{\omega_k d} \tag{1}$$

and

$$\Delta c(\omega_k) = \frac{c(\omega_k)^2 \phi(\omega_k)}{\omega_k d}, \tag{2}$$

where $c_r(\omega_k)$ is the reference-model phase velocity, d is the difference in epicentral distances between the near and far stations and $\phi(\omega_k)$ is a function depending on the estimated sample-squared coherence (see WSJ08, Section 3.2, for further details).

The error bounds, $\Delta c(\omega_k)$, are not derived directly from the dispersion but rather from the hypothesis that the two signals at the far station position—the observed and the model-based propagated waveform from the near station—are the same. The error bound on the phase is projected onto the calculated interstation dispersion with the caveat that the dispersion variation is all due to propagation (R.B. Herrmann, personal communication, 2008).

We compute the average phase velocity for a region at selected frequencies, ω_k, by averaging the individual interstation phase velocities that have interstation paths with centres within that region, scaled by the inverse of their coherency-derived standard deviations ($\Delta c(\omega_k)$ in eq. 2). The estimated phase-velocity errors are the observational standard deviations calculated from the phase velocities for all paths at that frequency. Appendix has a discussion of the statistics used in our phase-velocity analysis.

2.2 Phase-velocity maps

The phase velocity calculated for each interstation path using eq. (1) can be interpreted as the average phase velocity for that path. For preparing our contour plots, we use the geographical centre of the path as the reference location for that path (Fig. 1b). The path-midpoint location differs from that used in other phase-velocity mapping programs, such as 2-plane-wave modelling

(2PW; Yang & Ritzwoller 2008; Yang *et al.* 2008; Wagner *et al.* 2010). For each event, 2PW models the observed waveforms as the sum of two distinct Rayleigh-wave plane waves, each with its own amplitude, phase and backazimuth. One designates a reference station within the study area, and the method then calculates differences in wavefront-predicted and observed phase and amplitude between the reference station and all other stations to determine 2-D phase velocities throughout the study area. The assigned location for each interstation path is necessarily at the non-designated station. Note that 2PW assumes a single 2PW wavefield for all paths for each event, whereas our procedure treats each interstation path as independent. Another way to understand the difference in approaches is that 2PW could not be applied to arrivals from the Wells earthquake in our study region because at such short epicentral distances, the wavefronts cannot be approximated as plane waves (the GCPs in Fig. 1 are far from parallel), whereas our procedure makes no assumptions about the wavefront beyond (1) the requirement that acceptable interstation paths differ by no more than 3° from the epicentre-far-station GCP, and (2) the propagation between the two stations is along that path. In principle, we could choose any point along the path, but using path centres provides the best internal consistency.

To interpret the plots at each period, we consider and compare two measures of the error: the observational standard deviation (σ) discussed above and a quantity we define as the *average error* and denote by s. As shown in Appendix, s depends only on the coherency-derived individual-path estimated errors ($\sigma(\omega_k)$), so as coherency decreases, s increases.

Our 2-D maps use the local gridding algorithm *nearneighbor* from the GMT package (Wessel & Smith 1991; Wessel 2013), which uses a nearest-neighbor algorithm to assign a data value to each node only if there are data points within a circle of designated radius R centred at that node. We use the option that the algorithm will assign a value to that node only if there is at least one data point in all four quadrants. The algorithm employs an inverse-distance weighting scheme and allows for an additional user-input weight, for which we use the inverse of the coherency-derived estimated error (Δc) for that data point. If there is more than one data point for a quadrant within R of a node, the value of only the nearest datum will be used in calculating the average value for that node. We use a radius of 100 km and a gridding interval of 20 km.

3 SURFACE-WAVE ANALYSIS AT SMALL EPICENTRAL DISTANCES

WSJ08's surface-wave analysis assumed observations at teleseismic distances, which allowed a surface wave to be modelled as a steady-state wave with a constant horizontal wavenumber. However, at regional distances, GCPs are not parallel (Fig. 1) and, therefore, the wavefield cannot be modelled as a superposition of plane waves. This rules out approaches such as 2PW, but our two-station approach, with a limited range in backazimuths for the two stations, does not depend on the shape of the wavefront.

Additional assumptions about, for example, acceptable periods for the analysis are based on a far-field approximation and need to be checked. Lebedev *et al.* (2005, p. 995) suggest that, '[t]o ensure the validity of the far-field approximation, the minimum frequency [be] set such that at least 3–4 wavelengths of the fundamental mode at that frequency fit between the source and the station'. For our most distant station, COR at 787 km (Fig. 1a), this criterion suggests a maximum period of ~70 s. However, many of our stations have

epicentral distances less than a third of that to COR and we want to determine the maximum periods they can be used for this data set.

3.1 Synthetics

To assess the effect of small epicentral distances on the applicability of our analysis procedures, we generate vertical-component synthetics waveforms for the Wells earthquake at stations with interstation-path centres in our area of study. We use modal summation to create the synthetic waveforms (Herrmann 2013) based on the Group 2 velocity model from WSJ08 and the CMT values for location, group delay, and focal mechanism (using values found through http://www.globalcmt.org/CMTsearch.html).

We compute synthetic data sets both for a single (fundamental) mode and also for the first 100 modes. The calculated phase velocities for the two sets of synthetics do not differ significantly (Table 1), although the calculated errors are smaller for the fundamental-mode synthetics at shorter periods because of some interference from the first-higher mode in the 100-mode synthetics. Since the higher mode is observed in the data (Fig. 2b), we choose to use the 100-mode synthetics for our analysis despite the coherency method producing interstation Green's functions assuming a single mode. (The effect of the higher mode might be interpreted as contributing some 'noise' to our coherency analysis.)

Our limits in group velocity (2.0–4.0 km s^{-1}), period (4.0–128 s), and distance are determined from examination of FTAN plots (representative examples shown in Figs 2b and 3). For stations G04A (epicentral distance 764 km, Fig. 3a), H08A (epicentral distance 486 km, Fig. 3c) and ID007 (epicentral distance 209 km, Fig. 3b), the FTAN plots are well-behaved throughout the period range and give results consistent with the WSJ08 Group 2 velocity model used to calculate the synthetics up to ~100 s period. The first higher mode is clearly visible at the the two more distant stations (Figs 3a and c), less so at the nearest station (Fig. 3b), The higher-mode maxima are enough separated from the fundamental-mode maxima that we anticipate (and find) little interference. For stations with epicentral distances less than 200 km, the FTAN contour patterns lose coherency, so we did not include such stations in our analysis.

For the calculated interstation Green's function from the path between stations ID007 and H08A, the amplitude maxima for the fundamental mode are consistent with the Group 2 velocity model (Fig. 3d). A higher mode is not observed because our coherency calculation assumes a single mode (Jenkins & Watts 1968; Shumway 1988).

We applied the WSJ08 analysis procedure to the synthetic-waveforms database to estimate phase velocities at selected periods for each of the 188 interstation paths in our study area (centres shown in Fig. 1b). As an example of the results, Fig. 4 shows the phase-velocity spectra for two paths with similar backazimuths (1.9°, 1.8°) and interstation distances (282 km, 278 km), but different epicentral distances to the path centres (640 km, 383 km). For both paths, the estimated phase velocities agree well with the input model at shorter periods, but start to diverge at longer periods. The path at greater epicentral distance (OR057–COR) agrees with the input model to longer periods. For a fixed distance between the epicentre and path centre, varying the interstation distance has a negligible effect on the calculated phase velocities.

Because the synthetic waveforms are created using a 1-D velocity model, the calculated phase velocities should be laterally homogeneous throughout the study area. For periods shorter than ~32 s, the actual and calculated phase velocities are the same and the error
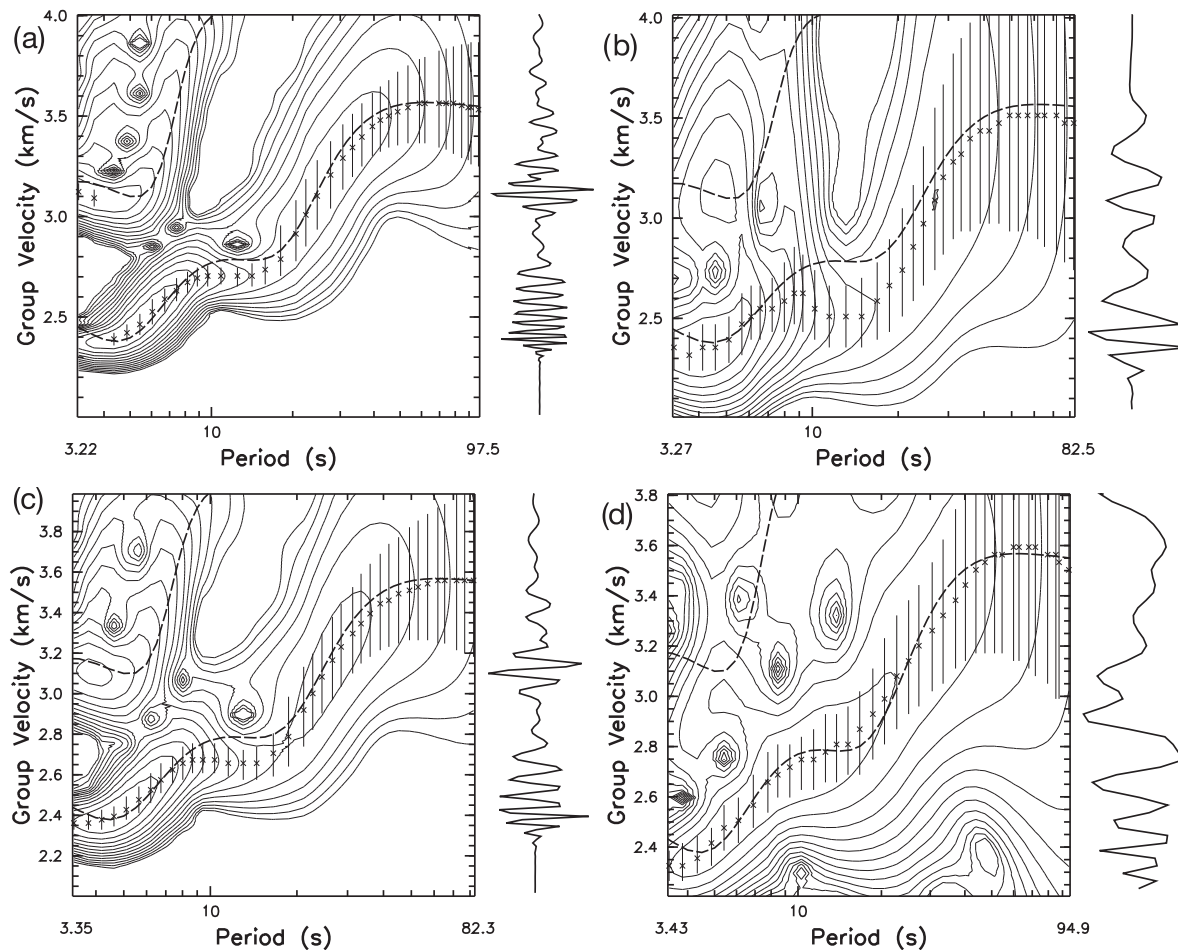
Figure 3. Group velocity versus period for the vertical-component 100-mode synthetics waveforms for the Wells earthquake (a) at station G04A with an epicentral distance of 765 km; (b) at station ID007 with an epicentral distance of 209 km; (c) at station H08A with an epicentral distance of 486 km; (d) interstation Green's function for the ID007–H08A station pair, with a path centre at an epicentral distance of 383 km and an interstation distance of 278 km. Station locations are shown in Fig. 1(a). As in Fig. 2(b), the dashed lines show the reference-model group-velocity curves for the Rayleigh-wave fundamental and first higher modes (not corrected for the depth or focal mechanism). The calculated group velocities have been corrected for a group delay of 2.5 s.

estimates are effectively zero for single-mode synthetics and less than 0.01 km s^{-1} for 100-mode synthetics (Table 1). Note that the phase-velocity map for 39.4 s (Fig. 5d) shows no hint of lateral heterogeneity and this lack of a pattern holds for smaller periods.

At longer periods, the measures of error increase with period (Table 1). At the longest periods, $\underline{s}$ is significantly larger than σ. Because the region is laterally homogeneous, a higher σ cannot be explained by poor signal-to-noise, lateral heterogeneity along the interstation path, or degraded data caused by multipathing. Rather, we suggest that these large values of σ and $\underline{s}$ result from limited coherency caused by distance/wavelength effects.

For periods of 73, 57, and 46.5 s, phase velocities increase systematically with epicentral distance (Figs 5a–c). For 73 s, the gradient is about 0.01 km s^{-1} in 60 km, and the gradient decreases by a factor of two at 57 s and an additional factor of 2 at 46.5 s. Note that σ for the three periods decreases at approximately the same rate as the gradients. We interpret the changes in σ as a measure of the apparent lateral heterogeneity caused by wavelength/distance effects. Note that at 46.5 s, σ is 0.003 km s^{-1}, which is much smaller than σ for teleseisms at any period (Table 1), so we feel we could use periods as long as 46.5 s in the analysis of the data.

Overall, these results are consistent with the spectra in Fig. 4: there is good agreement with the reference phase-velocity model at

shorter periods and variations at higher periods that depend on the epicentral distance of the path centres. We use these synthetics to develop empirical rules for applying our analysis procedures to the Wells earthquake data set. It is beyond the scope of this paper to explain the deviations at longer periods for shorter distances.

3.2 Guidelines for minimum epicentral distances and related constraints

A number of published studies provide guidelines for selecting minimum epicentral distances, the length of the signal to be analysed, and minimal lengths of interstation paths:

(1) **Minimum epicentral distances**: As mentioned earlier, Lebedev *et al.* (2005) recommend at least 3–4 wavelengths between the source and station. Our plots show that the analysis can produce good results to 40–50 s periods using stations with epicentral distances as small as 200 km, which is just over one wavelength.

(2) **The length of the signal to be analysed**: Wielandt & Schenk (1983, Page 4) say that '[n]ormally we set the window length to 200 s + 2T, at period T...', whereas D. W. Forsyth (personal communication, 2005) suggests a less restrictive guideline: 'The tapered
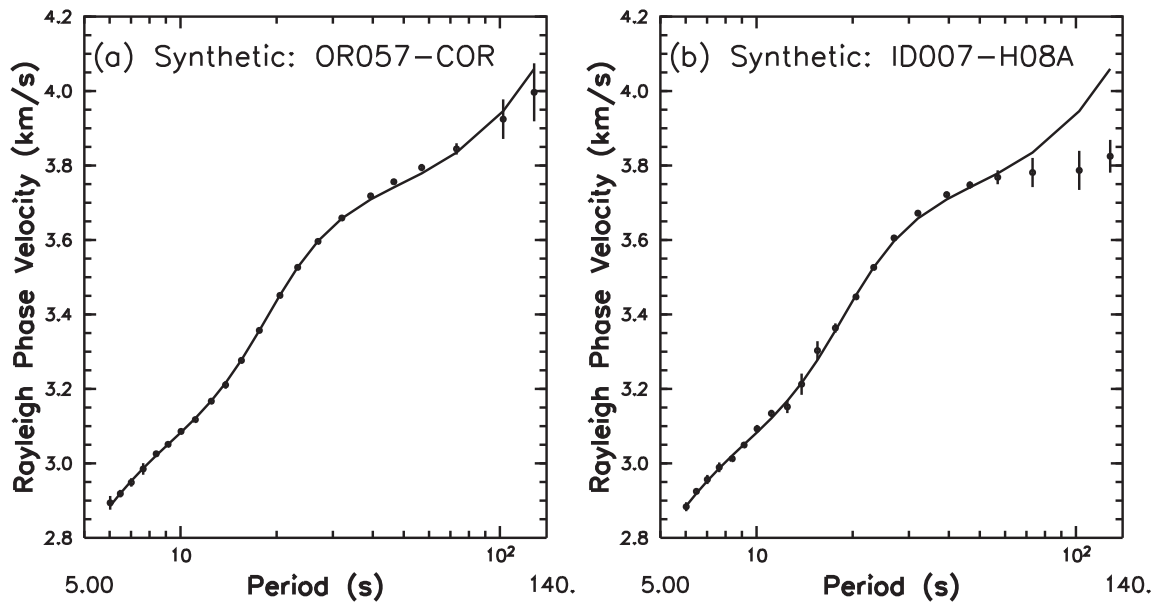
Figure 4. Synthetic interstation phase-velocity estimates as a function of period for the two interstation paths shown in Fig. 1(a), (a) OR057-COR and (b) ID007-H08A. The solid line is the phase-velocity curve for the velocity model used to create the synthetics. The path centres for (a) and for (b) are shown in Fig. 5.
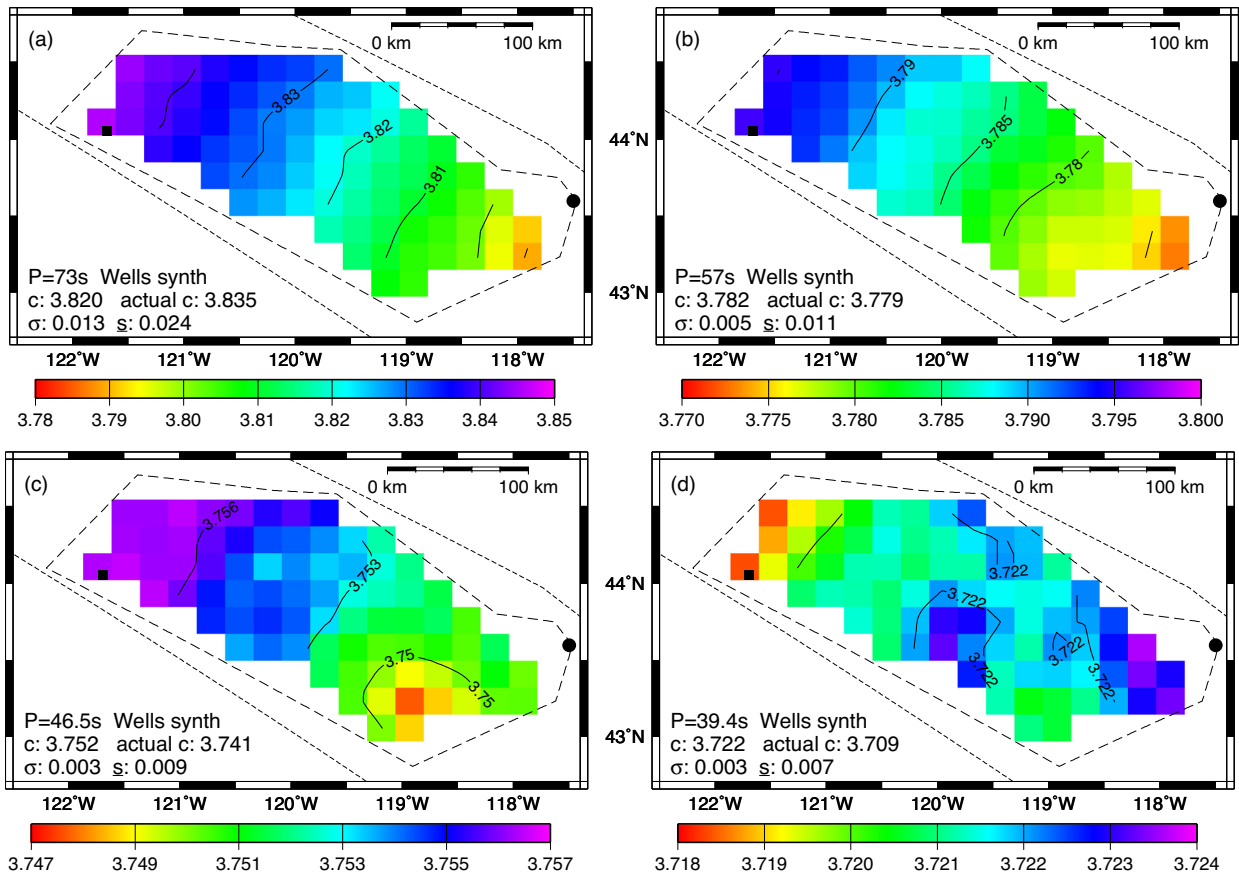

Figure 5. Contoured phase velocities for the Wells earthquake using 100-mode synthetics waveforms at the periods specified on the plots. The thin dashed lines mark the boundaries of WSJ08 Group 2, our study area. The thick dashed line bounds the 188 interstation-path centres (Fig. 1b). Centres for the two paths used in Fig. 4 are plotted as a square for OR057-COR and a circle for ID007-H08A. The epicentre of the Wells earthquake is at 114.87°W and 41.15°N, so epicentral distance increases towards the northwest. Text on each subplot gives the reference-model phase velocity at that period, the calculated average phase velocity, its standard deviation, and the average error estimate (from Table 1).
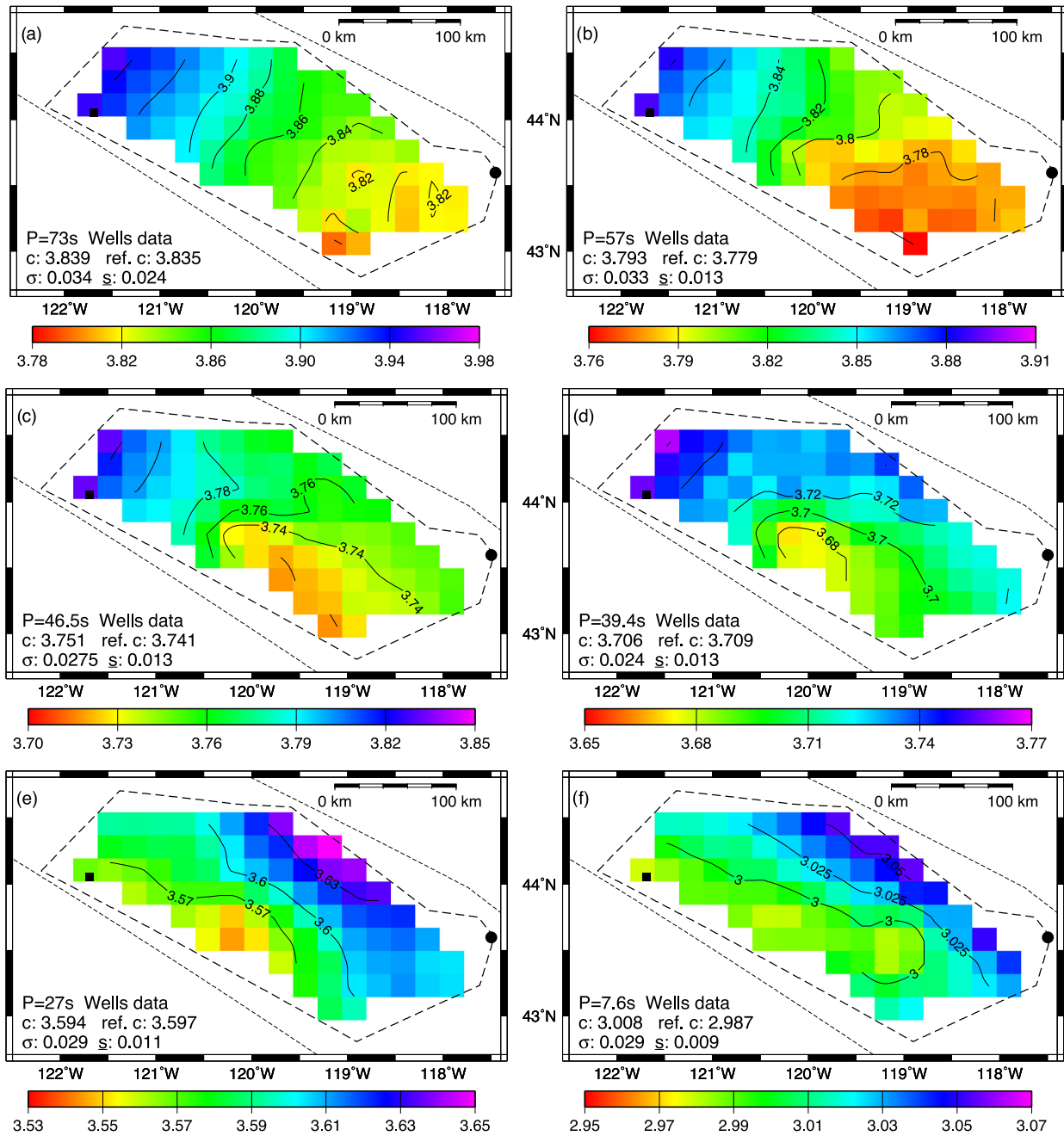
Figure 6. Contoured phase velocities for the Wells earthquake using data waveforms at the periods specified on the plots. The thin dashed lines mark the boundaries of WSJ08 Group 2, our study area. The thick dashed line bounds the 188 interstation-path centres (Fig. 1b). Centres for the two paths used in Fig. 4 are plotted as a square for COR057-COR and a circle for ID007-H08A. The epicentre of the Wells earthquake is at 114.87°W and 41.15°N, so epicentral distance increases towards the northwest. Text on each subplot includes the reference-model phase velocity at that period, the calculated average phase velocity, its standard deviation, and the average error estimate (from Table 1).

window length is the same for all stations and always greater than three times the desired period'.

As discussed in Section 2.1, WSJ08 used the well-constrained group-velocity range determined using FTAN plots to set the time limits for waveforms to be analysed. Using similar procedures, our chosen time window for the Wells earthquake corresponds to group velocities of 2.0–4.0 km s^{-1}. After adding a 15 per cent cosine taper at each end, the record lengths for this data set range from 70 to 250 s. If we followed Wielandt & Schenk's selection criterion, analysis would not be allowed at stations for which the time window

is less than 200 s. The robustness of our results show that at least for our method of analysis, we can work with waveforms slightly shorter than Forsyth's less-restrictive criterion.

(3) **Minimum interstation distance**: As with our modelling procedure, ambient noise tomography (ANT; Yang & Ritzwoller 2008; Yang *et al.* 2008; Hanson-Hedgecock *et al.* 2012; Wagner *et al.* 2012) works with interstation paths. Bensen *et al.* (2007) give a minimum interstation distance that is used by many others: the interstation distance must be at least three wavelengths of the wave at the target period. They assume a phase velocity of 4 km s^{-1}, so
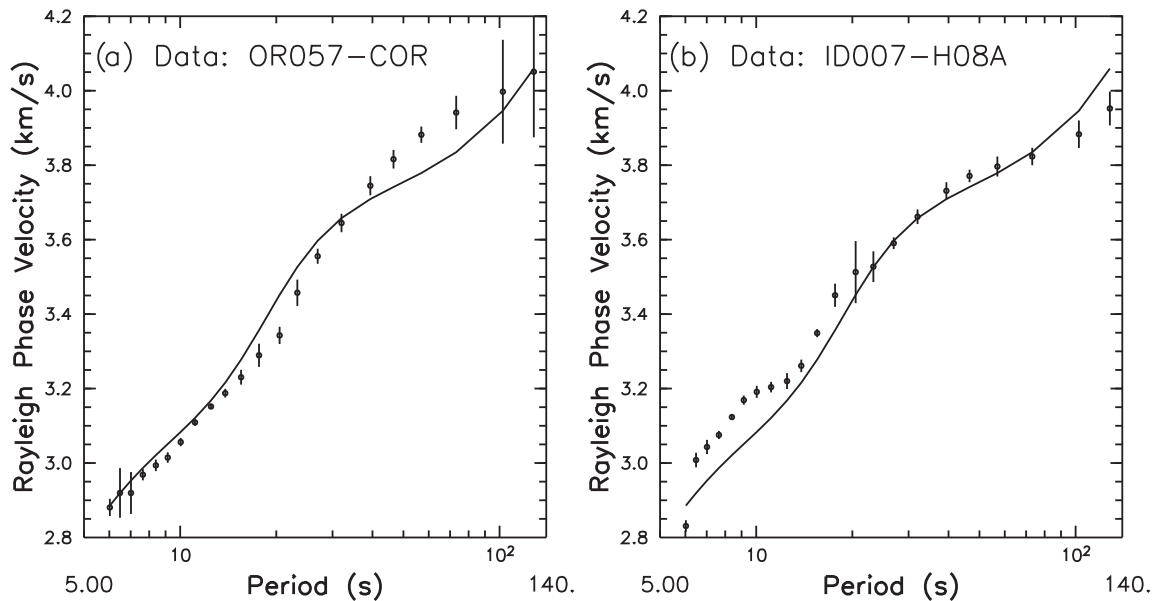
Figure 7. Interstation phase-velocity estimates as a function of period as in Fig. 4 but for the real data. The solid line is the phase-velocity curve for the reference model. The path centres for (a) and for (b) are shown in Fig. 6.

if the target period is T, the minimum interstation distance for that period is 12T in km.

Our synthetic tests indicate that for our method of processing, we get acceptable results at interstation distances down to 200 km. For 32 s period and a phase velocity of $3.66 \, \mathrm{km \, s^{-1}}$, the wavelength is 117 km, so 200 km is less than two wavelengths.

4 PHASE VELOCITIES FROM THE 2008 WELLS EARTHQUAKE: REAL DATA

The analysis of synthetic waveforms presented above indicates that our analysis procedures can be applied to surface waves at regional epicentral distances for periods up to $\sim$50 s. An important difference between the analyses for real and synthetic data is that the Group 2 model phase velocities are the actual phase velocities for the synthetics but only a reference set of phase velocities for the real data.

The estimated average phase velocities for the Wells earthquake ('Wells Data' in Table 1) agree well with the reference-model phase velocities for periods shorter than 60 s. Note that the reference-model phase velocities are unconstrained for periods shorter than 16 s because the data on which that model is based had a lower limit of 16 s period.

2-D phase-velocity maps (Fig. 6) constructed from the Wells earthquake data show lateral variability. For the two longest periods (73 s, 57 s; Figs 6a–b), the high σ and $\underline{s}$ values and the contours would, for teleseismic data, be interpreted as indicative of lateral heterogeneity. However, because of the synthetic results for these periods (Figs 5a–b), we interpret the apparent lateral heterogeneity as primarily caused by the small-distance effects.

At shorter periods (39.4 s, 27 s, 7.6 s; Figs 6d–f), the phase-velocity maps have a strong gradient of increasing phase velocities from the southwest to the northeast. Since σ is significantly larger than $\underline{s}$ at these periods, we interpret the variations as true lateral heterogeneity within the region. The spatial variation as a function of period is also apparent in a comparison of the dispersion curves for individual paths along the southwest and northeast boundaries

of our study area (Fig. 7), with the velocities for the path along the southwest boundary being slower at shorter periods.

The 46.5 s period phase-velocity map (Fig. 6c) is a transition between the higher periods and lower periods, with small-distance effects superimposed on lateral heterogeneity.

For areas including our study region, but with coarser station spacing (TA stations but not HLP stations), Pollitz & Snoke (2010) applied the non-planar wavefield approach to the western U.S. The local wavefield was fit with a plane-wave term plus two non-plane-wave terms [the first three terms of eq. 10 of Pollitz & Snoke (2010)]. Their phase-velocity maps at shorter periods are consistent with those presented here, but have lower resolution due to the larger station spacing and a Gaussian smoothing distance of 50 km.

5 CONCLUDING REMARKS

Our analysis of seismograms recorded by HLP and TA stations from the 2008 Wells earthquake shows that surface-wave analyses can provide well-constrained estimates of phase velocities at short periods for regional earthquakes. The short epicentral distances restrict the analyses to shorter periods, but based on our tests with synthetic data, the restrictions are not as strict as cited by other researchers (Wielandt & Schenk 1983; Lebedev *et al.* 2005; Bensen *et al.* 2007). Shorter distances allow for analyses at the shorter periods that are recorded with good signal-to-noise ratio from regional earthquakes. Based on signal-to-noise ratios and FTAN plots, the minimum period of $\sim$16 s for teleseisms is reduced to $\sim$7 s for the regionally-recorded Wells earthquake. For a surface wave with a period τ in seconds, the maximum sensitivity depth is at about the value of τ in kilometres. Hence, our method provides constraints on structure in the upper-crust (depths of $\sim$7 km for the Wells earthquake) and mid-crust ($\sim$16 km for teleseismic data).

The short-period cut-off generally used for 2PW modelling is about 25 s, because of ringing in long-distance teleseisms (L.S. Wagner, personal communication, 2014), so 2PW provides little information for depths shallower than the lower crust.

ANT can be used at shorter periods, and one study (Hanson-Hedgecock *et al.* 2012) includes the same station set as our study.

Their fig. S1 contains 2-D phase-velocity maps for periods from 8 to 33 s for a region including our study area. Their grid spacing is similar to ours, but they use a different contour algorithm. Their contours are at $0.1 \, \text{km s}^{-1}$ intervals, and the trend is similar to ours, but our results are smoother and show the gradient more clearly.

While the higher station density provided by the full HLP deployment does not provide better average phase velocities for areas on the scale of our study area (Table 1), the results given in Sections 4 and 5 indicate that high-density data allow one to get reliable measures of lateral heterogeneity within areas down to 150 km by 300 km in extent.

REFERENCES

Bensen, G.D., Ritzwoller, M.H., Barmin, M.P., Levshin, A.L., Lin, F., Moschetti, M.P., Shapiro, N.M. & Yang, Y., 2007. Processing seismic ambient noise data to obtain reliable broadband surface wave dispersion measurements, *Geophys. J. Int.,* **169,** 1239–1260.

Dziewonski, A., Block, S. & Landisman, M., 1969. A technique for analysis of transient seismic signals, *Bull. seis. Soc. Am.,* **59,** 427–444.

Friederich, W., Wielandt, E. & Stange, S., 1994. Non-plane geometries of seismic surface wavefields and their implications for regional-scale surface-wave tomography, *Geophys. J. Int.,* **119,** 931–948.

Hanson-Hedgecock, S., Wagner, L., Fouch, M.J. & James, D.E., 2012. Constraints on the causes of mid-Miocene volcanism in the Pacific Northwest US from ambient noise tomography, *Geophys. Res. Lett.,* **39,** L05301, doi:10.1029/2012GL05110810.

Herrmann, R.B., 1991. *Computer Programs in Seismology,* St. Louis University, St. Louis.

Herrmann, R.B., 2013. Computer programs in seismology: an evolving tool for education and research, *Seis. Res. Lett.,* **84,** 1081–1088.

Jenkins, G.M. & Watts, D.G., 1968. Spectral Analysis and Its Applications, Chap. 10, Holden-Day Series, Emerson Adams Pr Inc.

Larson, A.M., Snoke, J.A. & James, D.E., 2006. S-wave velocity structure, mantle xenoliths and the upper mantle beneath the Kaapvaal craton, *Geophys. J. Int.,* **167,** 171–186.

Lebedev, S., Nolet, G., Meier, T. & van der Hilst, R.D., 2005. Automated multimode inversion of surface and S waveforms, *Geophys. J. Int.,* **162,** 951–964.

Levshin, A.L., Yanovskaia, T.B., Lander, A.V., Bukchin, B.G., Barmin, M.P., Ramikova, L.I. & Its, E.N., 1989. Surface waves in vertically inhomogeneous media, in *Surface Waves in a Laterally Inhomogeneous Earth,* pp. 131–182, ed. Keilis-Borok, V.I., Springer-Verlag.

Nyman, D.C. & Landisman, M., 1977. The display-equalized filter for frequency-time analysis, *Bull. seism. Soc. Am.,* **67,** 393–404.

Pollitz, F.F. & Snoke, J.A., 2010. Rayleigh-wave phase-velocity maps and three-dimensional shear velocity structure of the western US from local non-plane surface wave tomography, *Geophys. J. Int.,* **180**(3), 1153–1169.

Shumway, R.H., 1988. *Applied Statistical Time Series Analysis,* Prentice Hall.

Snoke, J.A. & James, D.E., 1997. Lithospheric structure of the Chaco and Paraná Basins of South America from surface-wave inversion, *J. geophys. Res.,* **102,** 2939–2951.

Snoke, J.A. & Sambridge, M., 2002. Constraints on the S-wave velocity structure in a continental shield from surface-wave data: comparing linearized least-squares inversion and the direct-search neighbourhood algorithm, *J. geophys. Res.,* **107,** doi:10.1029/2001JB000498.

Wagner, L.S., Forsyth, D., Fouch, M. & James, D., 2010. Detailed three-dimensional shear wave velocity structure of the northwestern United States from Rayleigh wave tomography, *Earth planet. Sci. Lett.,* **299,** 273–284.

Wagner, L.S., Fouch, M.J., James, D. & Hanson-Hedgecock, S., 2012. Crust and upper mantle structure beneath the Pacific Northwest from joint inversions of ambient noise and earthquake data, *Geochem. Geophys. Geosyst.,* **13,** doi:10.1029/2012GC04353.

Warren, L.M., Snoke, J A. & James, D.E., 2008. S-wave velocity structure beneath the High Lava Plains, Oregon, from Rayleigh-wave dispersion inversion, *Earth planet. Sci. Lett.,* **274,** 121–131.

Wessel, P., 2013. GMT4 Online Services, Available at: http://gmt.soest.hawaii.edu/ (last accessed July 2013).

Wessel, P. & Smith, W.H.F., 1991. Free software helps map and display data, *EOS, Trans. Am. geophys. Un.,* **72,** 441.

Wielandt, E. & Schenk, H., 1983. On systematic errors in phase-velocity analysis, *J. geophys.,* **52,** 1–6.

Yang, Y.M. & Ritzwoller, H., 2008. Teleseismic surface wave tomography in the western US using the Transportable Array component of USArray, *Geophys. Res. Lett.,* **35,** L04308, doi:10.1029/2007GL032278.

Yang, Y., Ritzwoller, M.H., Lin, F.-C., Moschetti, M.P. & Shapiro, N.M., 2008. The structure of the crust and uppermost mantle beneath the western US revealed by ambient noise and earthquake tomography, *J. geophys. Res.,* **113,** B12310, doi:10.1029/2008JB005833.

APPENDIX A: PHASE-VELOCITY STATISTICS

Here, we discuss the statistics for fundamental-mode Rayleigh wave phase velocities (c) at fixed frequencies calculated using the coherency of earthquake-generated vertical-component waveforms recorded at a set of stations in a regional network. The forward-modelling method assumes that the phase velocity is uniform along each interstation path, but does not require that the velocities are the same for all paths. Hence, within the region spanned by the station network, the method potentially allows for the determination of lateral variations in phase velocity. We examine below the statistics for the average value and standard deviation of c.

For a single earthquake, there are N interstation paths satisfying the selection criterion (interstation distance at least 200 km and with a difference in interstation and far-station backazimuths less than $3°$). For each station i (i runs from 1 to N), we calculate c_i and its estimated standard deviation s_i. To calculate the statistics, we use weighted least squares with data scaled by the inverse of the estimated errors ($w_i = 1/s_i$). With this definition of w_i, the data

covariance matrix is proportional to the identity matrix. The average phase velocity for this data set is

$$\bar{c} = \frac{\sum_{j=1}^{N} w_j c_j}{\sum_{j=1}^{N} w_j} = \frac{\sum_{j=1}^{N} \frac{c_j}{s_j}}{\sum_{j=1}^{N} \frac{1}{s_j}}, \tag{A1}$$

and the standard deviation of the observations is

$$\sigma = \sqrt{\frac{\sum_{j=1}^{N} \left[\frac{c_j - \bar{c}_j}{s_j}\right]^2}{\sum_{j=1}^{N} \left[\frac{N-1}{s_j^2}\right]}}. \tag{A2}$$

There are alternatives in the literature to both our choice of w_i and the definition of the standard deviation to be used in the data analysis:

(1) **Optimal weights**: It can be shown that the 'optimum' weight is $w_i = 1/s_j^2$, because that choice gives the minimum value in the standard deviation of the average value $\bar{c}$.

(2) **Standard deviation of the mean**: To calculate the optimal weight, one must use the standard deviation of the mean rather than the standard deviation of the observations. This is given by

$$\bar{\sigma}^2 = \sum_{j=1}^{N} \left[\frac{\partial \bar{c}}{\partial c_j}\right]^2 s_j^2 = \frac{\sum_{j=1}^{N} w_j^2 s_j^2}{\sum_{j=1}^{N} w_j^2}. \tag{A3}$$

For our choice of w_i,

$$\bar{\sigma}^2 = \frac{N}{\left[\sum_{j=1}^{N} \frac{1}{s_j}\right]^2}. \tag{A4}$$

If one chooses to use $w_i = s_i^{-2}$, $\bar{\sigma}^2 = 1/\sum_{j=1}^{N} s_j^2$.

The line of reasoning in favour of using $\bar{\sigma}$ instead of σ in analyzing data is that the standard deviation of the observations gives us the answer if we had N observations and wanted to estimate the error we would have if we made only a single observation. Assuming that the N observations are all estimates of the same quantity, $\bar{c}$ is the best estimate of that quantity and $\bar{\sigma}$ is the appropriate measure of the error.

As stated above, a phase velocity is calculated for each inter-station path and phase velocity may vary within the study region. Hence, the assumptions made in deriving both the standard deviation of the mean and the optimal weights are not valid. For our study, eq. (A3) is the appropriate measure of the variation of the phase velocity within the region.

For a potentially heterogeneous data set, there is another problem with eq. (A4): if all the s_i were the same, for either choice of w_i $\bar{\sigma}$ decreases with $\sqrt{N}$. Hence, $\bar{\sigma}$ depends on the number of observations and does not reflect accurately a measure of actual heterogeneity within the region.

We find $\bar{\sigma}$ useful for comparing results for different periods or for data sets from different earthquakes: As $\bar{\sigma}$ depends only on the s_i (and not the c_i), $\bar{\sigma}$ is an interesting measure of how the calculation of c changes with period or at fixed period from event to event. To use it that way, we would need to keep N constant. Instead, we take out the N dependence by multiplying eq. (A4) by N. We call this measure the average error:

$$\underline{s} = \frac{N}{\sum_{j=1}^{N} \frac{1}{s_j}}, \tag{A5}$$

and include it, along with σ, in Table 1. The interpretation of these variables is discussed in Sections 3 (synthetics) and 4 (regional-earthquake data).